

Adaptive optics design for high-energy kW-class multi-slab laser amplifier

Tomáš Paliesek^{1,2}, Martin Divoký¹, Jan Pilař¹, Martin Smrž¹, and Tomáš Mocek¹

¹*HiLASE Centre, Institute of Physics of the Czech Academy of Sciences, Za Radnicí 828, 252 41 Dolní Břežany, Czech Republic*

²*Faculty of Nuclear Sciences and Physical Engineering, Czech Technical University in Prague, Břehová 7, 115 19 Prague, Czech Republic*

Abstract

We demonstrate real-time wavefront correction in a high-energy high-average-power DiPOLE100/Bivoj laser using adaptive optics. A bimorph deformable mirror and Shack-Hartmann wavefront sensor reduced wavefront error tenfold and improved the Strehl ratio elevenfold. Design aspects such as deformable mirror actuator geometry, optimal placement, and loop frequency are discussed for integration into next-generation high-energy high-average-power lasers.

Keywords: High-average-power laser, high-energy laser, wavefront correction, real-time adaptive optics

1. Introduction

DiPOLE laser architecture [1] has become an established laser source in the field of high-energy high-average power (HEHAP) diode-pumped solid state lasers (DPSSL), with 3 installations in the world [2, 3, 4]. The broad adjustability of its output parameters (1–150 J@1030 nm, 2–10 ns, 1–10 Hz) makes it suitable for diverse applications.

The very first system (known as Bivoj laser system) was delivered in 2015 to the HiLASE laser center (Dolní Břežany, Czech Republic), commissioned in 2016, and in recent years has achieved multiple world records [2, 5, 6]. It is used mainly for industrial applications (laser shock peening [7] and laser-induced damage threshold testing [8]) and for the research of space-oriented applications (space debris removal [9, 10] and spacecraft propulsion).

The second system was supplied to EU-XFEL (Hamburg, Germany) as a laser source for dynamic laser compression experiments at the high energy density instrument [11]. The third system is being installed at the Extreme Photonics Applications Center (Oxfordshire, UK) as a pump source for the Ti:Sapphire amplifier. The second harmonic frequency (515 nm) will be used to produce 1 PW pulses at a frequency of 10 Hz. In the future, two 100 J amplifiers will be installed here [12]. With recent progress in laser-driven inertial confinement fusion [13, 14], the DiPOLE architecture might be considered a potential fusion driver [15].

All of these applications require a high-quality beam in both near and far fields, which is often difficult to maintain because of various degrading effects that decrease the beam quality along the amplification path. Correcting for these effects and achieving the best beam parameters have become an indistinguishable aspect of laser development [16, 17, 18].

This paper investigates wavefront aberration correction in the second main amplifier of the Bivoj laser system through three key aspects: aberration characterization, simulation-based adaptive optics design, and experimental testing of the proposed solution. The turbulent cooling introduces random wavefront distortions, while the high average power of the amplifier causes strong static aberration with steep gradients around beam edges that complicate the wavefront sensor (WFS) and wavefront corrector (WFC) placement. Although an AO system was part of the original design, it failed to deliver a flat wavefront at the output of the laser.

1.1. Adaptive optics in high-power lasers

Many AO systems have been integrated into low-average-power lasers around the world [19, 20, 21, 22, 23, 24, 25, 26, 27]. The low average power (on the order of a few tens of watts maximum) is a consequence of either a very low repetition rate or low energy per pulse. Such output parameters imply rather low thermal loading of gain media, which results in aberration sources coming mainly from optics imperfections or external sources (for example, room

Correspondence to: Email: tomas.paliesek@hilase.cz

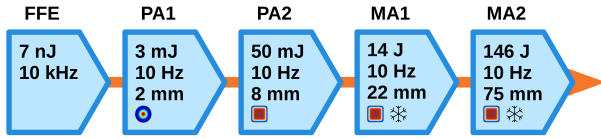


Figure 1: Schematics of the individual stages of the Bivoj laser system. FFE – Fiber front-end, MA – main amplifier, PA – preamplifier.

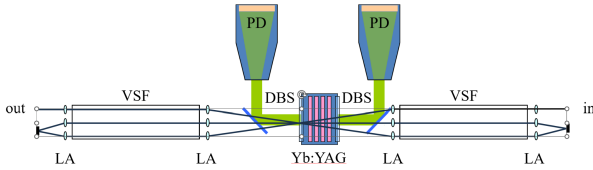


Figure 2: Schematics of the multi-pass architecture of the MA1 amplifier. PD – pump diodes, DBS – dichroic beam splitter, LA – lens array, VSF – vacuum spatial filter. Source: [30].

air turbulences). Recently, real-time aberration correction in a high-power laser was achieved [28], where an AO setup similar to that used in astronomy was employed.

Regarding the DiPOLE laser architecture, four similar laser systems have been developed (see the comparison in Table 1). Higher average power usually means a higher thermal loading of the gain media, higher temperature gradients, and therefore higher thermally induced aberrations. Moreover, a higher thermal load requires advanced cooling techniques, which are usually the source of other aberrations that are more random in character. To the best of our knowledge, the only work to date that addresses aberration correction in this type of laser system is [29]; however, it does not provide information on the temporal dynamics of the aberrations or the performance of adaptive optics.

Laser system	Pulse energy	Rep. rate	Pulse length	Avg. power
Bivoj [1, 2] (HiLASE)	146 J	10 Hz	2–10 ns	1460 W
Mercury [31] (LLNL)	55 J	10 Hz	14 ns	550 W
HAPLS [32, 33] (ELI Beamlines)	16 J	3.3 Hz	28.6 fs	53 W
HAPLS pump	97 J	3.3 Hz	20 ns	320 W
HELIA [34, 35] (Hamamatsu Photonics)	253 J 106 J	0.2 Hz 10 Hz	26 ns	51 W 1060 W
DiPOLE-100Hz [36] (STFC)	10 J	100 Hz	2–10 ns	1000 W

Table 1: High-energy high-average-power lasers comparison.

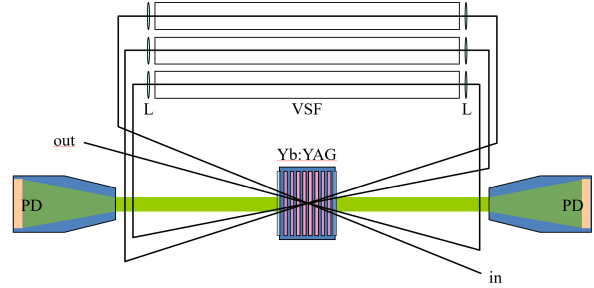


Figure 3: Schematics of the MA2 amplifier multi-pass architecture. PD – pump diodes, VSF – vacuum spatial filter, L – lens. Source: [30].

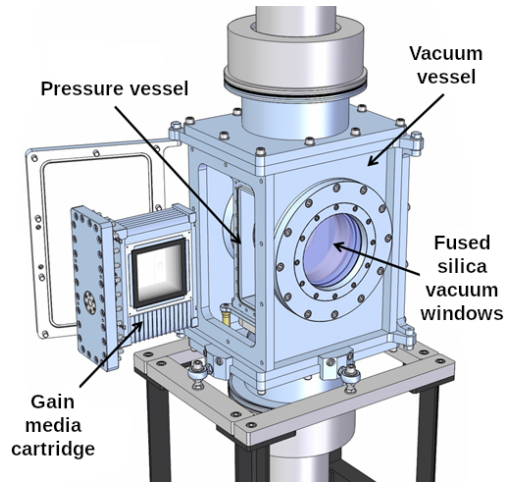


Figure 4: MA2 amplifier head model. Reprinted with permission from [1].

2. Bivoj laser system

Bivoj laser system consists of the front-end followed by two main cryogenically cooled multi-pass amplifiers (Fig. 1). The front-end consists of two preamplifiers and generates pulses with energy up to 50 mJ, frequency of 10 Hz, variable pulse shape, variable pulse length (2–10 ns) and adjustable beam profile.

The first main amplifier head (MA1) includes a set of four Yb:YAG gain disks. The pulse passes the gain media seven times using relay-imaging angular multiplexing geometry with a vacuum spatial filter after each pass, as shown in Fig. 2). After third pass, the deformable mirror (DM) compensates aberrations in the feedback loop with the wavefront sensor placed at the end of the amplifier. Then the beam transport section expands the beam from 22 mm × 22 mm to 75 mm × 75 mm and directs it to the second main amplifier, including optical isolation.

The second main amplifier (MA2) subsequently boosts the pulse energy to 146 J. The circular design shown in Fig. 3 features an amplifier head with six square-shaped variably-doped Yb:YAG slabs. The cooling helium gas flows through 2 mm wide gaps between slabs (see Fig. 4) and

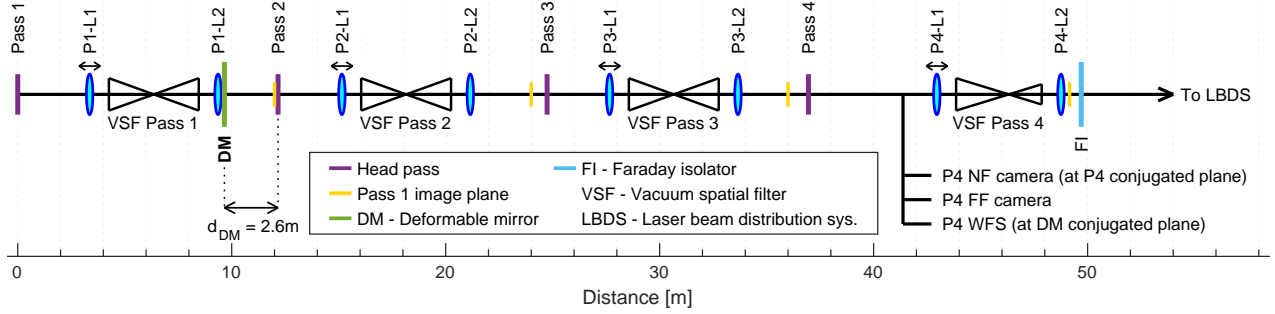


Figure 5: Original line scheme of the MA2 amplifier.

the operating temperature is 120–150 K. Two pump units deliver energy from the both sides of the head. The beam passes the head four times. Relay imaging on each pass is provided by a Keplerian telescope with 3 m long lenses and a vacuum spatial filter (VSF) with 3 mm pinhole in the common focal plane to suppress stray light. It is necessary to mention that the relay imaging distances are not precisely followed and each subsequent head plane drifts slightly from the respective image plane (explained in Sect. 2.1).

After the first VSF, a deformable mirror is used to compensate for thermal aberrations within the amplifier in the original design. The DM is controlled by a feedback loop with a WFS that samples mirror leak of the output beam. The DM position and performance are thoroughly explained in the following sections. A more detailed description of the DiPOLE laser architecture can be found in [1, 37].

2.1. Imaging scheme

Relay imaging is utilized in the whole laser system. The object plane is set by the spatial light modulator (SLM) in the front-end of the system [17] and the image plane is subsequently re-formed by relay telescopes at:

- The second preamplifier head,
- Each head pass of the MA1 amplifier (2x at every pass),
- MA1 Faraday isolator,
- The first head pass of MA2 amplifier.

However, this is not followed in the MA2 amplifier, as can be seen in Fig. 5. The yellow lines represent the single conjugated planes of the first MA2 head pass. The third head pass is located 74 cm away and the fourth head pass is 95 cm away from the first-pass conjugated plane. The deformable mirror is located 2.6 m before the second head pass, and the wavefront sensor is placed in the diagnostic line before the fourth VSF in the DM conjugated plane. The thermal lens in the amplifier head is compensated for by shifting the first VSF lens at each pass (marked with horizontal arrows above the lenses in Fig. 5).

3. Aberration characterization

The aberration sources in HEHAP multi-slab multi-pass amplifiers have already been identified [38, 39] and can be divided according to their dynamics:

- Static:
 - Heating by pumping,
 - Optics defects or imperfections,
- Dynamic:
 - Cooling,
 - Room air conditioning,
 - Head window blow.

Heating of the gain media is caused by 2 processes. Firstly, by non-radiative transitions after absorbing the pump radiation in the central part of the Yb:YAG slabs and, secondly, by amplified spontaneous emission absorption by the Cr:YAG cladding.

The subsequent aberration description refers to the operation at 100 J level with a cooling flow rate of 130 g/s and the gain media temperature of 150 K. The thermally induced defocus is compensated by moving the first telescope lens at each VSF and is equivalent to a thermal lens focal length of 234 m. The thermal equilibrium stabilizes around 30 s after the pump diodes are turned on.

The static component of aberration has a square geometry due to the gain-media shape, as can be seen in Fig. 6a. The profiles in Fig. 6b show that the gradients are steepest near the edges of the beam. Usually, when the amplifier is operated at 100 J-level, the output wavefront has STD value of 0.4–0.6 λ and peak-to-valley (PtV) of 3–4 λ (after the defocus is compensated). This results in a Strehl ratio of around 0.15 and a very distorted far-field image, as shown in Fig. 6d.

The dynamic sources of aberration are random in character. The rapid turbulent helium gas flowing in between aerodynamically shaped gain media vanes (Reynolds number >19000) efficiently cools each gain media face. The MA2 beam path is only partially covered and therefore the room air-conditioning also contributes to fluctuations. The amplifier head windows must be under

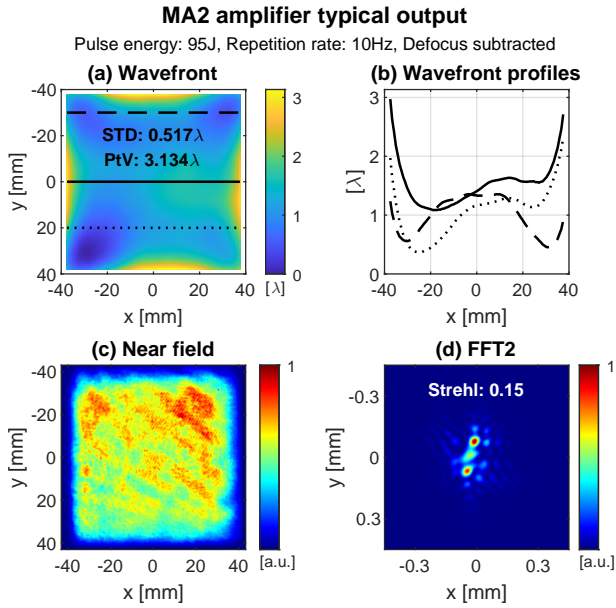


Figure 6: MA2 typical output beam shape and wavefront with subtracted defocus. Line profiles show steep gradients near beam edges.

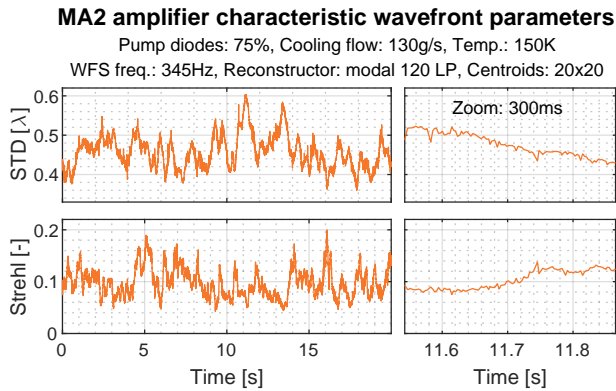


Figure 7: Evolution analysis of aberration parameters for the MA2 amplifier.

constant flow of nitrogen gas to avoid condensation of air humidity when the amplifier is cooled down.

The evolution of the wavefront parameters is presented in Fig. 7. The data show no periodic changes, the pulse-to-pulse stability of STD was within 0.04λ . To further quantify the effects that degrade wavefront quality, the continuous wave (CW) alignment beam (1030 nm, single-mode laser diode) was propagated through the amplifier at various settings and wavefront evolution over a period of 100s was measured. The measurements involved changing temperature, cooling helium gas flow, and pumping power. The original deformable mirror was removed from the amplifier and replaced by a plane mirror.

The results can be observed in Fig. 8. Simply propagating the beam through the non-cooled amplifier decreases the Strehl ratio to 0.45. The standard deviation (STD) of the

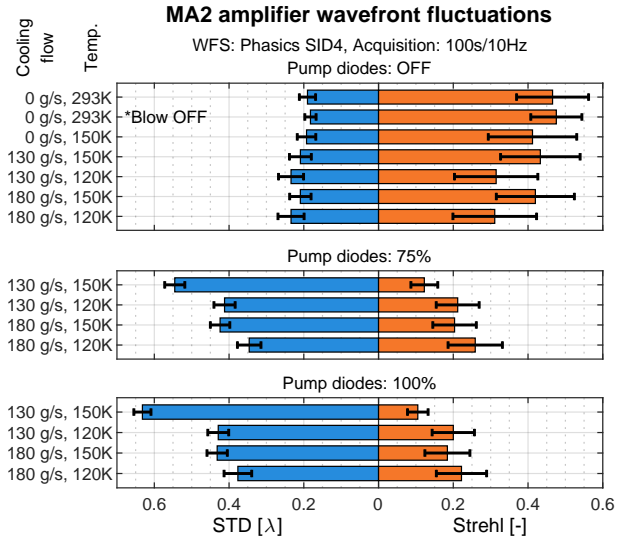


Figure 8: MA2 amplifier wavefront STD and Strehl fluctuations analysis for various amplifier settings.

Strehl is around 50% lower when the head window blow is turned off at room temperature. After the head is cooled down and the cooling flow is turned off, the Strehl decreases even more (~ 0.4), and the Strehl fluctuations increase by 20%.

A 75% pumping rate simulates operation at an output energy of 100 J, where 25% of the absorbed energy is extracted by the output pulses. The 100% pumping rate corresponds to operation at the 150 J level, in which the pumping power is increased by approximately 25% above the standard 100 J operation parameters, and the head temperature is decreased to 120 K. The pumping power increases the STD values and decreases the Strehl ratio mainly due to thermal loading. The cooling power is increased by raising the flow rate, which also increases fluctuations. However, a higher helium flow rate reduces the STD and increases the Strehl ratio. Both parameters reach improved values at a temperature of 120 K, which is likely due to the thermo-mechanical properties of YAG – its thermal conductivity increases and its thermo-optic coefficient decreases as the temperature lowers [40].

4. Adaptive optics design considerations

The following section analyzes the original AO design and discusses why it was unable to reach flat wavefront at the output of the amplifier. The subsequent subsections propose new requirements for the AO system (AO repetition rate, DM position, and DM geometry) using simulations based on the wavefront evolution measurements data.

4.1. Original AO design

The original amplifier design includes a piston-actuated large-aperture deformable mirror ILAO 135x95 with 52

actuators (ISP System, France), located 20 cm after the second lens of the first-pass VSF at 45° incidence angle (see Fig. 5). The positioning was determined by the size of the mirror, the lack of relay image planes, and the low energy fluence after the first head pass. The MA2 output diagnostic line uses the 0° mirror leak before passing the last VSF and reduces the beam to $2\text{ mm} \times 2\text{ mm}$. The Phasics SID4 WFS is positioned in conjugated plane of the deformable mirror.

To evaluate the performance of the DM, a test bench was built. The reflected wavefront of the ILAO DM in its flat state reached an STD of 17 nm over a beam aperture of $75\text{ mm} \times 75\text{ mm}$. The DM was also able to replicate the inverse thermal aberration to that in Fig. 6a up to 58 nm STD error. Despite this performance, the AO loop was unable to converge to a flat wavefront at the amplifier output, as was mentioned before. Eventually, we identified two main reasons for this behavior: the deformable mirror location and the long actuator rise time.

After the test bench evaluation, the ILAO DM was returned to the amplifier according to the original design. With cooling turned off and at room temperature (no strong aberrations present in the amplifier head), the ILAO DM was able to achieve a wavefront STD error of 167 nm. Compared to the case without the DM of 190 nm (see Fig. 8), this presents a limited improvement. The deformable mirror compensates for optics imperfections but is too slow to address the dynamic aberration component. The repetition rate depends on the maximum actuator stroke change and one period typically takes 1–5 s.

When the cooling and pumping are on, the original AO system performance was worse. The best achieved wavefront STD was around 270 nm. In this case, also the deformable mirror position in relation to the aberration source plane plays an important role, which is explained in Sect. 4.3.

4.2. AO repetition rate

To determine what AO repetition rate is necessary to achieve a flat wavefront, the wavefront evolution at the MA2 amplifier output was measured using a high-speed Shack-Hartmann WFS, and correction simulation was performed to investigate how varying the loop frequency affects the system's ability to compensate for dynamic wavefront distortions.

The correction was simulated on the wavefront evolution acquired at a frame rate of 300 Hz and following amplifier settings: 75 % pumping, a cooling flow rate of 130 g/s, and a temperature of 150 K. The influence functions (i.e., the responses of individual actuators) of the 8×8 -actuator square deformable mirror were used to apply the correction by subtraction. These influence functions were chosen because this mirror was available for testing at our facility. The correction was computed only at specific frames, depending on the correction frequency, and was applied by subtracting

it from the current frame and all subsequent frames. The correction accounted for loop gain but did not consider actuators' limited ranges.

Depending on the loop gain and the number of eigen modes used in the simulation, to achieve the mean Strehl value higher than 0.8, the required AO repetition rate of 20–40 Hz was necessary and at least full 300 Hz was required to reach the mean Strehl higher than 0.9. These results were confirmed in the experiment, where the DM at the output of the system was used to compensate for aberrations at various repetition rates (see Sect. 5 and Fig. 16).

4.3. DM location

The inability of the original AO design to converge to a flat wavefront led to investigation of the deformable mirror position in the MA2 amplifier. The first aspect is the imaging in the strongly perturbed environment of the laser amplifier, discussed in Sect. 4.3.1. The second aspect is relative positioning of the DM and the main aberration source, explained in Sect. 4.3.2.

4.3.1. Imaging DM plane to WFS plane: Adaptive optics systems typically position the WFC and WFS at planes within the optical system that are conjugated to its output pupil, as this conjugation is crucial for proper AO operation. In the MA2 amplifier case, the deformable mirror is conjugated to the wavefront sensor according to Fig. 5 in the original design. But they are not conjugated with the aberration source planes (head passes) and these aberrations strongly distort imaging from DM onto WFS, as can be seen from the following beam propagation simulation.

Let us now consider imaging the DM plane to the WFS plane in the diagnostic line, according to the original design presented in Fig. 5. By simulating the beam propagation in the amplifier, we found that the strong thermally-induced aberrations – mainly the strong gradients near the edges of the beam – severely distort the imaging. The reference cross imprinted in deformable mirror plane is intentionally moved near the edges of the beam, where the wavefront gradients are the steepest.

When pumping is on, the straight lines on the deformable mirror are no longer straight when imaged onto the WFS plane, as can be seen in Fig. 9. Therefore, the actuators' responses seen by the WFS are also deformed. The propagation model based on the angular spectrum method [41, 42] included free-space propagation, lenses, and aberrations at each head pass.

The simulation allowed to place an artificial DM plane anywhere in the MA2 amplification path. Fig. 10a shows less image distortion when the DM plane is placed closer to the second head pass. Nevertheless, even when $d_{\text{DM}} = 0\text{ m}$ (Fig. 10b) there are still some scintillation artifacts around the beam edges that are probably caused by the fact that the

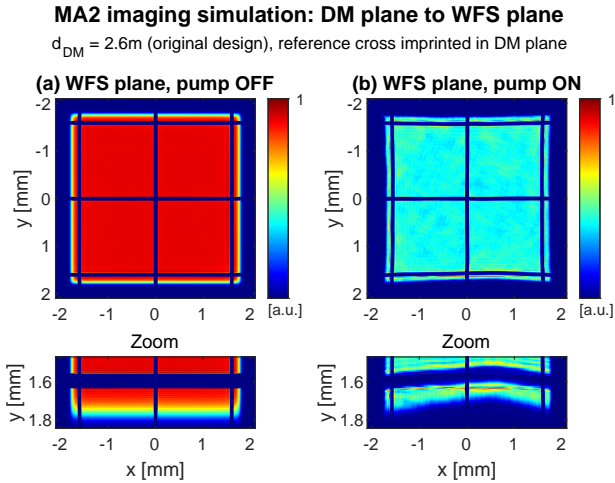


Figure 9: Simulation of imaging the DM plane onto the WFS plane in the MA2 amplifier. A beam with a reference cross imprinted in the DM plane is propagated through the MA2 model. The simulation scheme is shown in Fig. 5. Wavefront aberrations imposed at each head pass simulate pumping. The imaging is distorted in the presence of strong wavefront gradients that are not conjugated with the DM plane.

individual head passes are not perfectly conjugated, as was mentioned above. Following the simulation result, it would be beneficial to position the DM in a head conjugated plane. This is the case of the MA1 amplifier, where before and after each head pass, the image plane is reproduced and the DM is placed in the head conjugated plane after the third head pass (see Fig. 2). Unfortunately, this is not possible in the current MA2 setup as there are no image planes available for DM installation. An amplifier redesign would be in order.

4.3.2. Validity of geometric optics: Another point of view on this issue is whether the geometric optics (GO) validity is followed in the original MA2 amplifier layout. We will use the description given in [43], which explains the validity of GO for adaptive optics for astronomical telescopes.

This condition generally holds when diffraction is insufficient to produce significant intensity changes (scintillations) at the telescope pupil, which is often the case for aberration caused by weak turbulence. If this weak-turbulence condition is maintained, then light rays emanating from a single-point source can be corrected by placing the WFC at any point along the ray path. If not, interference effects become visible and the resulting phase and intensity variations cannot be completely removed.

This poses limits on where the WFC can be positioned, a topic that has been widely studied in the field of multi-conjugate adaptive optics for astronomy [44, 45] and conjugate adaptive optics for microscopy [46, 47]. The main idea of this concept is to place the wavefront correctors in planes conjugated to the aberration source layers and compensate for each aberration layer independently. This

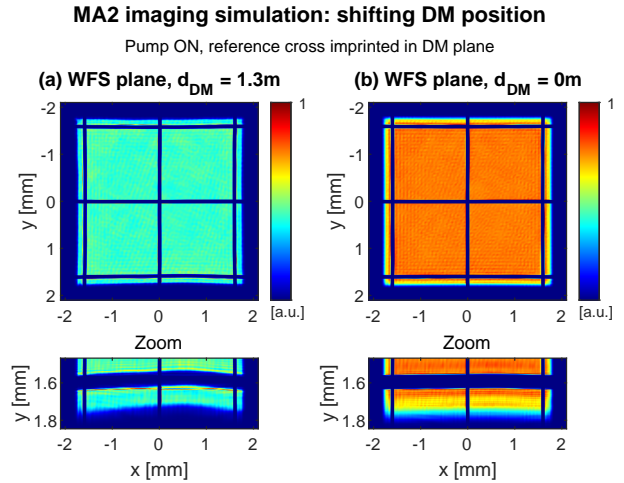


Figure 10: Simulation of imaging the DM plane onto the WFS plane in the MA2 amplifier, with the DM moved closer to the head (aberration source plane). The distance d_{DM} is defined in Fig. 5, which also shows the simulation scheme. The imaging is distorted due to strong wavefront gradients that are not conjugated with the DM. The closer the DM is to the head, the less distortion appears in the beam profile.

arrangement preserves the validity of geometric optics for wavefront correction and restores the spatial relation between the aberration layer and the WFC [43]. Otherwise, the rays at the WFC are displaced, making it impossible to fully compensate for the aberrations.

Light incident on the aberration layer (see Fig. 11) is diffracted at an angle δ equal to λ/ρ , where λ is the mean wavelength and ρ is the aberration layer scale size. Interference will occur when diffracted rays travel a distance comparable to:

$$h = \rho/\delta = \rho^2/\lambda. \quad (1)$$

If the propagation distance between the aberration layer and the WFC is less than h , the diffraction effects may be neglected and the wavefront aberrations can be compensated by placing the WFC at any location in the ray path. However, if the aberration is stronger, then the diffracted rays are displaced and produce interference effects. In astronomy, the characteristic size is given by Fried's parameter r_0 , which is the diameter over which the wavefront aberration has a mean square value of 1 rad^2 at a wavelength of $0.5 \mu\text{m}$.

Applying this description to the typical output wavefront of the MA2 amplifier, it can be found that the diameter of the area where the mean square wavefront error reaches 1 rad^2 differs from only 1.2 mm near the edge to 20 mm in the middle of the beam. If the minimum value is substituted into Eq. (1), it is found that the distance below which the validity of GO is maintained is $h = 1.4 \text{ m}$ if the WFC is placed at the MA2 output.

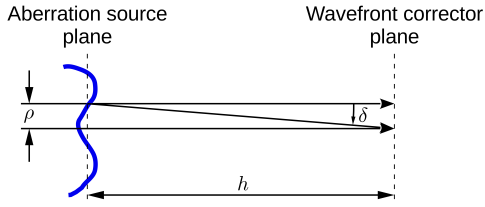


Figure 11: Aberrated beam interfere at the wavefront corrector when $h > \rho/\delta = \rho^2/\lambda$. Inspired by [43].

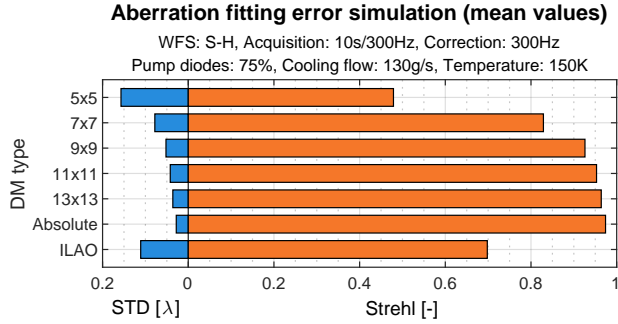


Figure 12: Aberration fitting error simulation for various DM geometries. The 300 Hz correction with different DMs was simulated at wavefront evolution data acquired with Shack-Hartmann WFS.

4.4. Aberration fitting error (estimation of spatial properties of a DM)

In order to estimate the requirements placed on DM actuators, the performance of several common actuator array distributions was analyzed and compared in a numerical study. The sample DMs corresponding to the selected designs were analyzed in terms of the response functions of all the estimated actuators. The temporal wavefront development subjected to correction was taken from the wavefront evolution measurements within MA2 done with the fast Shack-Hartmann WFS. The spatial distributions of the DM actuator arrays were regular square distributions of 5×5 , 7×7 , 9×9 , 11×11 , 13×13 actuators and the original ILAO DM actuator distribution (52 actuators).

The results for 300 Hz operation are shown in Fig. 12 together with the absolute correction result, which represents a result of direct application of the correction (not via actuator superposition) and therefore presents a limit of the correction given only by the limited temporal dynamics and correction gain of the estimated AO system. From the results it can be seen that, in order to address the expected wavefront aberrations, the square arrays perform better than ILAO DM geometry and that the required number of actuators should be at least 7×7 .

4.5. AO design conclusions

Table 2 summarizes the findings of the previous paragraphs. The required repetition rate implies using a piezoelectric

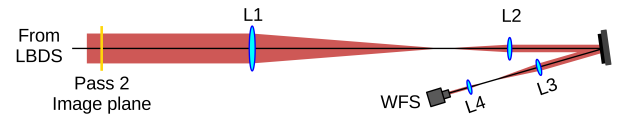


Figure 13: Test experiment scheme. The DM, WFS and second head pass plane are all conjugated. LBDS – laser beam distribution system, L1–L4 – lenses.

deformable mirror with kHz bandwidth featuring square geometry and a high frame rate wavefront sensor. The DM in the amplifier should be positioned as close as possible to the aberration source (conjugated) plane to mitigate the DM to WFS imaging distortion. If placed at the MA2 output, the distance from the aberration source conjugated plane should be less than 1.4 m.

AO repetition rate	
Mean Strehl > 0.8	20–40 Hz
Mean Strehl > 0.9	300 Hz
DM distance from aberration source (conjugated) plane	
DM at the output	< 1.4 m
DM inside the amp.	0 m (DM in conjugated plane)
DM geometry	
Geometry	Square
# of actuators	min. 7×7

Table 2: MA2 amplifier AO design summary.

5. Experimental AO performance

Based on all considerations, simulations and space limitations, it was decided to place the deformable mirror at the second head pass conjugated plane at the amplifier output and test the aberration correction. The 8×8 bimorph DM with clear aperture of $22 \text{ mm} \times 22 \text{ mm}$ was used. The wavefront sensor was Shack-Hartmann, capable of a 500 Hz frame rate when aperture is cropped to 100 centroids. The control software as well as the DM and WFS were supplied by Dynamic Optics. The amplifier parameters were set to reproduce the thermal loading during 100 J operation (pumping power: 75 %, cooling flow rate: 130 g/s, temperature: 150 K).

The MA2 output laser beam was delivered by the laser beam distribution system (LBDS) to the testing setup. The $75 \text{ mm} \times 75 \text{ mm}$ beam was demagnified by a telescope and imaged onto the DM, which was placed in the second head pass conjugated plane. The Following telescope re-imaged the DM onto WFS. Fig. 13 illustrates the experiment arrangement. The beam covered 20×20 microlenses on the

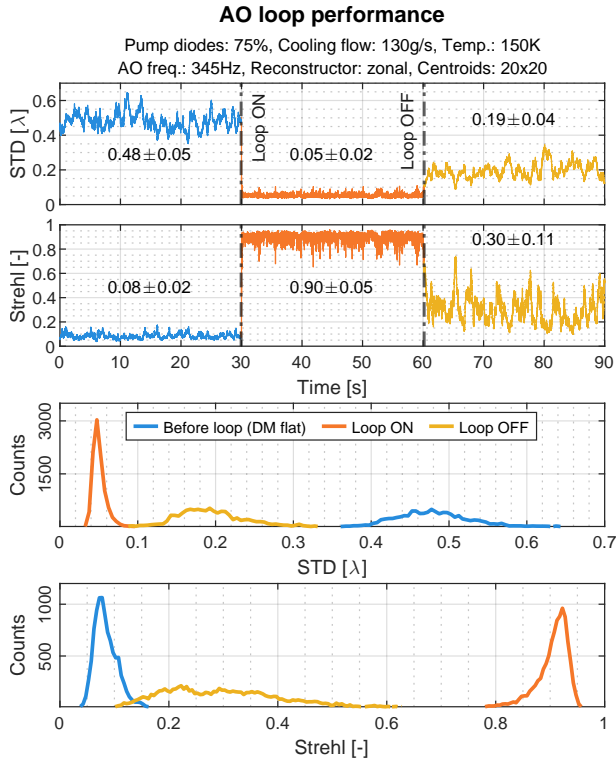


Figure 14: Adaptive optics setup performance at 345 Hz. First two line plots show evolution of STD and Strehl, last 2 plots present STD and Strehl value histograms.

wavefront sensor, which allowed us to operate the WFS at a frame rate of 345 Hz.

Initially, the actuators were set to their zero positions and after 30 s, the AO loop was started. The loop settling time to reach the Strehl ratio of 0.9 was 62 ms (21 iterations) at a repetition rate of 345 Hz. After another 30 s, the AO loop was stopped to observe aberrations evolution with static correction applied at DM. The performance is presented in plots in Fig. 14. The wavefront STD was improved by 10× and the Strehl ratio by 11× when the loop was turned on. After stopping the loop, the static correction improved the Strehl ratio only 4× and STD 2.5×, mainly because of the dynamic nature of the aberrations. The sample wavefronts for each measurement sections are shown in Fig. 15 together with individual far-field distributions.

Fig. 16 shows AO performance at different repetition rates. The repetition rate necessary to achieve the mean Strehl of 0.8 was 50 Hz. The repetition rate of 345 Hz allowed us to exceed the Strehl ration of 0.9. The results are in good agreement with the simulations results. It should be noted that the AO loop did not take into account changes of pointing because tilt stability was influenced by the long beam path through the laser beam distribution system to the testing setup area and therefore does not correspond to the pointing stability at the output of the amplifier.

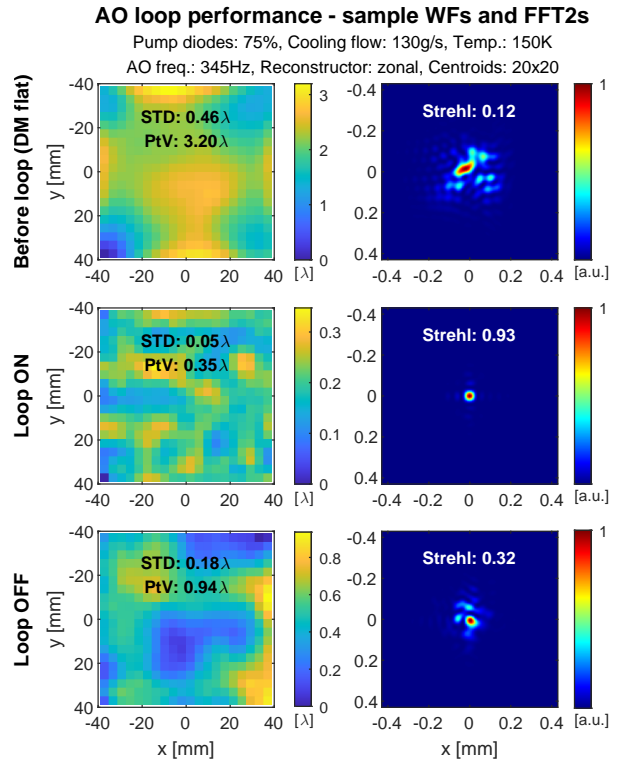


Figure 15: Sample wavefronts for individual stages of the AO setup performance shown in Fig. 14.

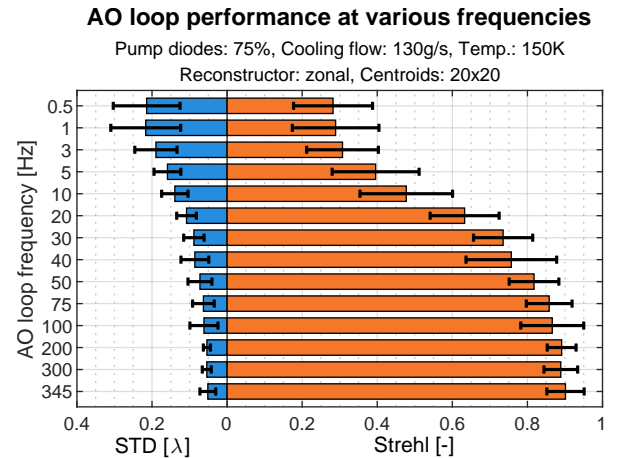


Figure 16: Adaptive optics setup performance at various loop frequencies. Mean values when the AO loop was on are displayed.

6. Discussion

The results show that aberration correction in MA2 is possible. However, the deformable mirror will have to be placed as close as possible to the head conjugated plane either before the beam enters the MA2, inside MA2, or less than 1.4 m away from the head conjugated plane at the output. In addition, a probe beam will have to be added to the amplifier chain, allowing the AO system to work at high frame rates.

The first option would require a DM for $22\text{ mm} \times 22\text{ mm}$ beam that withstands a fluence of 3.2 J/cm^2 (which might be challenging for large apertures [48]) or redesign the beam transport section that connects the MA1 and MA2 amplifiers, while maintaining the current MA1 output beam size and image plane, which is often used separately. If the DM was placed inside the MA2, a MA2 redesign would be required, as well as a large aperture DM (for $75\text{ mm} \times 75\text{ mm}$ beam) that could operate in kHz bandwidth. The last option would also require the same type of DM as option 2 except with a higher damage threshold specification ($>2\text{ J/cm}^2$).

7. Conclusion

In summary, this paper investigates the design of the adaptive optics system for the high-energy high-average-power Bivoj laser with possible impact on all DiPOLE100 architecture lasers worldwide. In order to determine necessary parameters of the AO system, aberrations characterization was carried out. The aberration composition is unique because high average power implies a strong static component, and turbulent cooling adds a strong random character. To the best of our knowledge, no other works on this type of aberration correction have been published. What makes it more difficult is that the presence of strong wavefront gradients restricts positioning of deformable mirror.

The test experiment showed a successful aberration correction at the output of the MA2 amplifier. The AO setup used the 8×8 -actuator bimorph deformable mirror, Shack-Hartmann wavefront sensor, and PhotoLoop control software (Dynamic Optics, Italy). The wavefront STD was improved $10\times$ and the Strehl ratio $11\times$ when the AO loop was turned on with a repetition rate of 345 Hz. However, due to high AO repetition rate needed, the experiment was performed at low output energy, only with the CW alignment beam. The position of a deformable mirror was discussed throughout the article from the point of view of conjugation with aberration source plane and also from the point of view of original design limitations.

It was found that the original design with a piston-actuated large aperture deformable mirror would not be able to achieve acceptable wavefront parameters even though it was located in a more suitable position. The repetition rate of the mirror would limit the correction performance because of the dynamic nature of the aberration.

An important contribution of this work is for the new DiPOLE-100Hz [36] laser system that is currently being evaluated in our center. The thermal loading and the cooling-induced aberration will be comparable, but the beam aperture will be $22\text{ mm} \times 22\text{ mm}$, making the wavefront gradients even stronger.

Data availability statements

The data that support the findings of this study are openly available in Zenodo repository at <https://doi.org/10.5281/zenodo.16612166>.

Acknowledgements

This work was co-funded by the European Union and the state budget of the Czech Republic under the project LasApp CZ.02.01.01/00/22_008/0004573.

Disclosures

The authors declare no conflict of interest.

References

- [1] Saumyabrata Banerjee et al. "100 J-level nanosecond pulsed diode pumped solid state laser". In: *Optics Letters* 41.9 (May 1, 2016), p. 2089. issn: 0146-9592, 1539-4794. doi: 10.1364/OL.41.002089. url: <https://www.osapublishing.org/abstract.cfm?URI=ol-41-9-2089> (visited on 01/03/2022).
- [2] Martin Divoký et al. "150 J DPSSL operating at 1,5 kW level". In: *Optics Letters* 46.22 (Nov. 15, 2021), p. 5771. issn: 0146-9592, 1539-4794. doi: 10.1364/OL.444902. url: <https://www.osapublishing.org/abstract.cfm?URI=ol-46-22-5771> (visited on 12/14/2021).
- [3] Paul Mason et al. "Progress on Commissioning a 10 Hz Petawatt Laser at the Extreme Photonics Applications Centre". In: (2024).
- [4] Luke McHugh et al. "Commissioning a high-energy 10Hz Ti:Sa amplifier for the petawatt laser at the Extreme Photonics Applications Centre". In: *Solid State Lasers XXXIV: Technology and Devices*. Solid State Lasers XXXIV: Technology and Devices. Ed. by W. Andrew Clarkson and Ramesh K. Shori. San Francisco, United States: SPIE, Mar. 21, 2025, p. 12. doi: 10.1117/12.3041937. url: <https://www.spiedigitallibrary.org/conference-proceedings-of-spie/13341/3041937/Commissioning-a-high-energy-10Hz-Ti-Sa-amplifier-for-the/10.1117/12.3041937.full> (visited on 05/29/2025).
- [5] Martin Divoky et al. "Kilowatt-class high-energy frequency conversion to 95 J at 10 Hz at 515 nm". In: *High Power Laser Science and Engineering* 11 (2023), e65. issn: 2095-4719, 2052-3289. doi: 10.1017/hpl.2023.60. url: https://www.cambridge.org/core/product/identifier/S2095471923000609/type/journal_article (visited on 11/23/2023).

- [6] Jan Pilar et al. “Half-kilowatt high-energy third-harmonic conversion to 50 J @ 10 Hz at 343 nm”. In: *High Power Laser Science and Engineering* 12 (2024), e96. issn: 2095-4719, 2052-3289. doi: 10.1017/hpl.2024.80. url: https://www.cambridge.org/core/product/identifier/S209547192400080X/type/journal_article (visited on 07/02/2025).
- [7] D. Rostohar et al. “How new laser development can help laser shock peening penetration to widen industrial applications?” In: *2017 IEEE 3rd International Forum on Research and Technologies for Society and Industry (RTSI)*. 2017 IEEE 3rd International Forum on Research and Technologies for Society and Industry - Innovation to Shape the Future for Society and Industry (RTSI). Modena, Italy: IEEE, Sept. 2017, pp. 1–4. isbn: 978-1-5386-3906-1. doi: 10.1109/RTSI.2017.8065959. url: <http://ieeexplore.ieee.org/document/8065959/> (visited on 02/08/2022).
- [8] Pavel Cech et al. “LASER INDUCED DAMAGE THRESHOLD TESTING AT HILASE”. In: *MM Science Journal* 2019.5 (Dec. 11, 2019), pp. 3657–3661. issn: 18031269, 18050476. doi: 10.17973/MMSJ.2019.12.2019118. url: <http://www.mmscience.eu/2019118> (visited on 06/13/2025).
- [9] Séverine A. E. Boyer et al. “On the performance of high-power pulsed repeated laser irradiation for spatial structures propulsion”. In: *High-Power Laser Ablation VIII*. High-Power Laser Ablation VIII. Ed. by Claude R. Phipps and Vitaly E. Gruzdev. Santa Fe, United States: SPIE, Sept. 26, 2024, p. 38. isbn: 978-1-5106-7976-4. doi: 10.1117/12.3012647. url: <https://www.spiedigitallibrary.org/conference-proceedings-of-spie/PC12939/3012647/On-the-performance-of-high-power-pulsed-repeated-laser-irradiation/10.1117/12.3012647.full> (visited on 01/06/2025).
- [10] Stefan Scharring et al. “Orbital re-focusing of high energy laser beams from ground for laser-ablative post-mission disposal and debris removal”. In: *Proc. 9th European Conference on Space Debris*. European Conference on Space Debris. Bonn, Germany: ESA Space Debris Office, Apr. 2025. url: <https://conference.sdo.esoc.esa.int/proceedings/sdc9/paper/140/SDC9-paper140.pdf> (visited on 07/01/2025).
- [11] *XFEL: New DiPOLE laser blasts off*. July 5, 2023. url: https://www.xfel.eu/news_and_events/news/index_eng.html?openDirectAnchor=2123 (visited on 04/24/2025).
- [12] *CLF EPAC Pump Laser*. url: <https://www.clf.stfc.ac.uk/Pages/EPAC-Pump-Laser.aspx> (visited on 04/24/2025).
- [13] *National Ignition Facility - 2024*. June 13, 2025. url: <https://annual.llnl.gov/fy-2024/national-ignition-facility-2024>.
- [14] H. Abu-Shawareb et al. “Lawson Criterion for Ignition Exceeded in an Inertial Fusion Experiment”. In: *Physical Review Letters* 129.7 (Aug. 8, 2022), p. 075001. issn: 0031-9007, 1079-7114. doi: 10.1103/PhysRevLett.129.075001. url: <https://link.aps.org/doi/10.1103/PhysRevLett.129.075001> (visited on 06/03/2025).
- [15] Antonio Lucianetti et al. “Design of a kJ-class HiLASE laser as a driver for inertial fusion energy”. In: *High Power Laser Science and Engineering* 2 (May 1, 2014), e13. issn: 2095-4719, 2052-3289. doi: 10.1017/hpl.2014.15. url: https://www.cambridge.org/core/product/identifier/S2095471914000152/type/journal_article (visited on 04/05/2022).
- [16] Ondřej Slezák et al. “Thermal-stress-induced birefringence management of complex laser systems by means of polarimetry”. In: *Scientific Reports* 12.1 (Oct. 31, 2022), p. 18334. issn: 2045-2322. doi: 10.1038/s41598-022-22698-9. url: <https://www.nature.com/articles/s41598-022-22698-9> (visited on 03/16/2023).
- [17] Tomáš Paliesek et al. “Beam shaping in the high-energy kW-class laser system Bivoj at the HiLASE facility”. In: *High Power Laser Science and Engineering* 11 (2023), e79. issn: 2095-4719, 2052-3289. doi: 10.1017/hpl.2023.79. url: https://www.cambridge.org/core/product/identifier/S2095471923000798/type/journal_article (visited on 02/15/2024).
- [18] Dominika Jochcová et al. “Power output optimization in complex laser systems by means of polarization control”. In: *Journal of Optics* 27.1 (Jan. 1, 2025), p. 015601. issn: 2040-8978, 2040-8986. doi: 10.1088/2040-8986/ad9619. url: <https://iopscience.iop.org/article/10.1088/2040-8986/ad9619> (visited on 07/04/2025).
- [19] Frédéric Druon et al. “Wave-front correction of femtosecond terawatt lasers by deformable mirrors”. In: *Optics Letters* 23.13 (July 1, 1998), p. 1043. issn: 0146-9592, 1539-4794. doi: 10.1364/OL.23.001043. url: <https://opg.optica.org/abstract.cfm?URI=ol-23-13-1043> (visited on 12/18/2024).
- [20] Richard A. Sacks et al. “Application of adaptive optics for controlling the NIF laser performance and spot size”. In: *Third International Conference on Solid State Lasers for Application to Inertial Confinement*

- Fusion. Ed. by W. Howard Lowdermilk. Monterey, CA, July 23, 1999, p. 344. doi: 10.1117/12.354146. URL: <http://proceedings.spiedigitallibrary.org/proceeding.aspx?doi=10.1117/12.354146> (visited on 04/28/2025).
- [21] H. Baumhacker et al. “Correction of strong phase and amplitude modulations by two deformable mirrors in a multistaged Ti:sapphire laser”. In: *Optics Letters* 27.17 (Sept. 1, 2002), p. 1570. ISSN: 0146-9592, 1539-4794. doi: 10.1364/OL.27.001570. URL: <https://opg.optica.org/abstract.cfm?URI=ol-27-17-1570> (visited on 12/18/2024).
- [22] B. Wattellier et al. “High-power short-pulse laser repetition rate improvement by adaptive wave front correction”. In: *Review of Scientific Instruments* 75.12 (Dec. 2004), pp. 5186–5192. ISSN: 0034-6748, 1089-7623. doi: 10.1063/1.1819379. URL: <http://aip.scitation.org/doi/10.1063/1.1819379> (visited on 12/02/2021).
- [23] Thomas A. Planchon et al. “Adaptive wavefront correction on a 100-TW/10-Hz chirped pulse amplification laser and effect of residual wavefront on beam propagation”. In: *Optics Communications* 252.4 (Aug. 2005), pp. 222–228. ISSN: 00304018. doi: 10.1016/j.optcom.2005.04.020. URL: <https://linkinghub.elsevier.com/retrieve/pii/S0030401805003433> (visited on 01/28/2025).
- [24] Federico Canova et al. “Wavefront correction and aberrations pre-compensation in the middle of Petawatt-class CPA laser chains”. In: Conference on Lasers and Electro-Optics (CLEO). Baltimore, USA, 2007. doi: 10.1109/CLEO.2007.4453292.
- [25] Dai Wanjun et al. “Beam wavefront control of a thermal inertia laser for inertial confinement fusion application”. In: *Applied Optics* 48.19 (July 1, 2009), p. 3691. ISSN: 0003-6935, 1539-4522. doi: 10.1364/AO.48.003691. URL: <https://opg.optica.org/abstract.cfm?URI=ao-48-19-3691> (visited on 06/02/2025).
- [26] Sensen Li et al. “Wavefront Shaping by a Small-Aperture Deformable Mirror in the Front Stage for High-Power Laser Systems”. In: *Applied Sciences* 7.4 (Apr. 11, 2017), p. 379. ISSN: 2076-3417. doi: 10.3390/app7040379. URL: <https://www.mdpi.com/2076-3417/7/4/379> (visited on 06/02/2025).
- [27] Deen Wang et al. “1178 J, 527 nm near diffraction limited laser based on a complete closed-loop adaptive optics controlled off-axis multi-pass amplification laser system”. In: *High Power Laser Science and Engineering* 9 (2021), e22. ISSN: 2095-4719, 2052-3289. doi: 10.1017/hpl.2021.3. URL: https://www.cambridge.org/core/product/identifier/S2095471921000037/type/journal_article (visited on 04/24/2025).
- [28] Jonas Benjamin Ohland et al. *Apollon Real-Time Adaptive Optics (ARTAO) – Astronomy-Inspired Wavefront Stabilization in Ultraintense Lasers*. Dec. 11, 2024. doi: 10.48550/arXiv.2412.08418. arXiv: 2412.08418[physics]. URL: <http://arxiv.org/abs/2412.08418> (visited on 12/18/2024).
- [29] Z. Liao. “Wavefront Correction on High Repetition Rate, High Energy Laser System”. In: The Advanced Maui Optical and Space Surveillance Technologies Conference. ADS Bibcode: 2006amos.confE..32L. Jan. 1, 2006, E32. URL: <https://ui.adsabs.harvard.edu/abs/2006amos.confE..32L> (visited on 06/03/2025).
- [30] M. Divoky et al. “Overview of the HiLASE project: high average power pulsed DPSSL systems for research and industry”. In: *High Power Laser Science and Engineering* 2 (May 1, 2014), e14. ISSN: 2095-4719, 2052-3289. doi: 10.1017/hpl.2014.16. URL: https://www.cambridge.org/core/product/identifier/S2095471914000164/type/journal_article (visited on 12/09/2021).
- [31] A. Bayramian et al. “The Mercury Project: A High Average Power, Gas-Cooled Laser for Inertial Fusion Energy Development”. In: *Fusion Science and Technology* 52.3 (Oct. 2007), pp. 383–387. ISSN: 1536-1055, 1943-7641. doi: 10.13182/FST07-A1517. URL: <https://www.tandfonline.com/doi/full/10.13182/FST07-A1517> (visited on 06/03/2025).
- [32] E. Sistrunk et al. “All Diode-Pumped, High-repetition-rate Advanced Petawatt Laser System (HAPLS)”. In: *Conference on Lasers and Electro-Optics*. San Jose, California: OSA, 2017, STh1L.2. ISBN: 978-1-943580-27-9. doi: 10.1364/CLEO_SI.2017.STh1L.2. URL: https://opg.optica.org/abstract.cfm?URI=CLEO_SI-2017-STh1L.2 (visited on 07/02/2025).
- [33] C. L. Haefner et al. “High average power, diode pumped petawatt laser systems: a new generation of lasers enabling precision science and commercial applications”. In: *Proc. SPIE 10241, Research Using Extreme Light: Entering New Frontiers with Petawatt-Class Lasers III, 1024102 (26 June 2017)*. SPIE Optics + Optoelectronics. Ed. by Georg Korn and Luis O. Silva. Prague, Czech Republic, June 26, 2017, p. 1024102. doi: 10.1117/12.2281050. URL: <http://proceedings.spiedigitallibrary.org/proceeding.aspx?doi=10.1117/12.2281050> (visited on 12/20/2021).
- [34] Takashi Sekine et al. “253 J at 0.2 Hz, LD pumped cryogenic helium gas cooled Yb:YAG ceramics laser”. In: *Optics Express* 30.25 (Dec. 5, 2022),

- p. 44385. ISSN: 1094-4087. DOI: 10.1364/OE.470815. URL: <https://opg.optica.org/abstract.cfm?URI=oe-30-25-44385> (visited on 06/03/2025).
- [35] Takaaki Morita et al. "Current status of the LD-pumped Yb:YAG ceramics laser toward 250J at 10Hz operation". In: *High Power Lasers for Fusion Research VIII*. High Power Lasers for Fusion Research VIII. Ed. by Constantin L. Häfner and Abdul A. Awwal. San Francisco, United States: SPIE, Mar. 21, 2025, p. 14. DOI: 10.1117/12.3042692. URL: <https://www.spiedigitallibrary.org/conference-proceedings-of-spie/13343/3042692/Current-status-of-the-LD-pumped-Yb-YAG-ceramics-laser/10.1117/12.3042692.full> (visited on 06/03/2025).
- [36] Mariastefania De Vido et al. "Demonstration of stable, long-term operation of a nanosecond pulsed DPSSL at 10 J, 100 Hz". In: *Optics Express* 32.7 (Mar. 25, 2024), p. 11907. ISSN: 1094-4087. DOI: 10.1364/OE.521049. URL: <https://opg.optica.org/abstract.cfm?URI=oe-32-7-11907> (visited on 09/26/2024).
- [37] M. Divoky et al. "Performance comparison of Yb:YAG ceramics and crystal gain material in a large-area, high-energy, high average-power diode-pumped laser". In: *Optics Express* 28.3 (Feb. 3, 2020), p. 3636. ISSN: 1094-4087. DOI: 10.1364/OE.379713. URL: <https://www.osapublishing.org/abstract.cfm?URI=oe-28-3-3636> (visited on 12/20/2021).
- [38] Jan Pilar et al. "Design and optimization of an adaptive optics system for a high-average-power multi-slab laser (HiLASE)". In: *Applied Optics* 53.15 (May 20, 2014), p. 3255. ISSN: 1559-128X, 2155-3165. DOI: 10.1364/AO.53.003255. URL: <https://opg.optica.org/abstract.cfm?URI=ao-53-15-3255> (visited on 07/11/2023).
- [39] Magdalena Sawicka-Chyla et al. "Numerical Analysis of Thermal Effects in a Concept of a Cryogenically Cooled Yb: YAG Multislab 10 J/100-Hz Laser Amplifier". In: *IEEE Journal of Quantum Electronics* 55.5 (Oct. 2019), pp. 1–8. ISSN: 0018-9197, 1558-1713. DOI: 10.1109/JQE.2019.2929962. URL: <https://ieeexplore.ieee.org/document/8766821/> (visited on 10/17/2024).
- [40] R. L. Aggarwal et al. "Measurement of thermo-optic properties of Y3Al5O12, Lu3Al5O12, YAlO3, LiYF4, LiLuF4, BaY2F8, KGd(WO4)2, and KY(WO4)2 laser crystals in the 80–300K temperature range". In: *Journal of Applied Physics* 98.10 (Nov. 15, 2005). Publisher: AIP Publishing. ISSN: 0021-8979, 1089-7550. DOI: 10.1063/1.2128696. URL: <https://pubs.aip.org/jap/article/98/10/103514/291744/Measurement-of-thermo-optic-properties-of-Y3Al5O12> (visited on 07/18/2025).
- [41] Joseph W. Goodman. *Introduction to Fourier optics*. 2nd ed. McGraw-Hill series in electrical and computer engineering. New York: McGraw-Hill, 1996. 441 pp. ISBN: 978-0-07-024254-8.
- [42] David George Voelz. *Computational fourier optics: a MATLAB tutorial*. Bellingham, Wash: SPIE Press, 2011. 232 pp. ISBN: 978-0-8194-8204-4.
- [43] John W. Hardy. *Adaptive optics for astronomical telescopes*. Oxford series in optical and imaging sciences 16. New York: Oxford University Press, 1998. ISBN: 978-0-19-509019-2.
- [44] J. M. Beckers. "Increasing the Size of the Isoplanatic Patch with Multiconjugate Adaptive Optics". In: 30 (Oct. 1, 1988). Conference Name: Very Large Telescopes and their Instrumentation, Vol. 2 ADS Bibcode: 1988ESOC...30..693B, p. 693. URL: <https://ui.adsabs.harvard.edu/abs/1988ESOC...30..693B> (visited on 03/19/2024).
- [45] François Rigaut and Benoit Neichel. "Multiconjugate Adaptive Optics for Astronomy". In: *Annual Review of Astronomy and Astrophysics* 56.1 (Sept. 14, 2018), pp. 277–314. ISSN: 0066-4146, 1545-4282. DOI: 10.1146/annurev-astro-091916-055320. URL: <https://www.annualreviews.org/doi/10.1146/annurev-astro-091916-055320> (visited on 03/20/2024).
- [46] Jörgen Thaug et al. "Dual-conjugate adaptive optics for wide-field high-resolution retinal imaging". In: *Optics Express* 17.6 (Mar. 16, 2009), p. 4454. ISSN: 1094-4087. DOI: 10.1364/OE.17.004454. URL: <https://opg.optica.org/oe/abstract.cfm?uri=oe-17-6-4454> (visited on 03/22/2024).
- [47] Jerome Mertz, Hari Paudel, and Thomas G. Bifano. "Field of view advantage of conjugate adaptive optics in microscopy applications". In: *Applied Optics* 54.11 (Apr. 10, 2015), p. 3498. ISSN: 0003-6935, 1539-4522. DOI: 10.1364/AO.54.003498. URL: <https://opg.optica.org/abstract.cfm?URI=ao-54-11-3498> (visited on 03/25/2024).
- [48] Zhi M. Liao and Thomas Spinka. "Small-beam damage test scaling for full-aperture damage performance". In: *Laser-Induced Damage in Optical Materials 2022*. Laser-Induced Damage in Optical Materials 2022. Ed. by Christopher W. Carr, Detlev Ristau, and Carmen S. Menoni. Rochester, United States: SPIE, Dec. 2, 2022, p. 68. DOI: 10.1117/12.2644342. URL: <https://www.spiedigitallibrary.org/conference-proceedings-of-spie/12300/2644342/Small-beam-damage-test-scaling-for-full-aperture-damage-performance/10.1117/12.2644342.full> (visited on 07/03/2025).